https://doi.org/10.5194/egusphere-2025-2579
Preprint. Discussion started: 31 July 2025

Extreme Glacier Melt in the Central Tibetan Plateau during the Summer of 2022: Detection and Mechanisms

Fei Zhu[1,2], Meilin Zhu[3]*, Lu An[1,2]

[1]College of Surveying and Geo-Informatics, Tongji University, Shanghai, 200092, China.

[2]Center for Spatial Information Science and Sustainable Development, Tongji University, Shanghai, 200092, China.

[3]Center for the Pan-Third Pole Environment, Lanzhou University, Lanzhou 730000, China.

Corresponding author: Meilin Zhu* (zhuml@lzu.edu.cn)

https://doi.org/10.5194/egusphere-2025-2579
Preprint. Discussion started: 31 July 2025

Abstracts

Extreme glacier melt events accelerate mass loss, increase glacier instability, and temporarily mitigate downstream drought. However, the glacier energy-mass balance in the Geladandong region—the headwater of both the Yangtze River (China's longest river) and Siling Co (Tibet's largest lake)—and its connection to the unprecedented 2022 summer melt remain insufficiently quantified. To address this gap, we integrated in situ mass balance observations (October 2019–July 2022) and glacio-meteorological data from a 5,700 m monitoring site (October 2020–July 2022) with a surface energy-mass balance model, and applied a novel dual-threshold framework (based on mean and standard deviation) to identify extreme mass loss/melt events in short-term glacier mass balance records. Our novel methodology identified 2021–2022 as a period of extreme mass loss and melt intensity, with melt during the 2022 summer heatwave reaching unprecedented extremes. Over 52 days, the heatwave generated 1,135 mm w.e. of melt—accounting for 65.2% of the total 2021–2022 melt, equivalent to 1.8 and 2.3 times the melt recorded in 2019–2020 and 2020–2021, respectively. This extreme melt was driven by energy balance anomalies over glacier surface, including reduced albedo, increased incoming longwave radiation, and enhanced sensible heat fluxes, with these processes strongly linked to persistent high temperatures and diminished precipitation. Such anomalies in the energy balance were driven by large-scale atmospheric circulation anomalies—specifically, the concurrent intensification and westward expansion of the Western Pacific Subtropical High (WPSH) and the eastward extension of the South Asian High (SAH). This study establishes a novel framework for identifying extreme mass loss events and substantially advances understanding of glacier mass balance responses to extreme weather and climate events.

Keywords: Energy and mass balance, Extreme heat waves, Extreme melt, Extreme mass loss

https://doi.org/10.5194/egusphere-2025-2579
Preprint. Discussion started: 31 July 2025

1. Introduction

Extreme glacier melt events directly reflect glacier mass balance responses to extreme weather and climate events, such as heatwaves, droughts, and wildfires. Given the increasing frequency of extreme glacier mass loss events across Tibetan Plateau (TP) and surrounding regions since the early 21st century, this short-term intensive depletion events significantly alter long-term glacier mass balance trends and increase risks of glacier-related geohazards (Yao et al., 2022; Immerzeel et al., 2020; You et al., 2020; Zhang et al., 2023b; Zhu et al., 2024b). In recent decades, scientific focus has increased on understanding spatiotemporal patterns and driving mechanisms of glacial retreat and thinning across TP (Bolch et al., 2012; Yao et al., 2012; Brun et al., 2017; Hugonnet et al., 2021). Studies have systematically revealed how atmospheric circulation patterns and dominant climate variables govern spatiotemporal variations in glacier mass balance across TP. Large-scale atmospheric anomalies generate distinct regional disparities in air temperature-precipitation regimes, potentially explaining the observed spatial heterogeneities in glacier mass balance (Yao et al., 2012). Meteorological controls exhibit strong regional differences: annual precipitation dominates mass balance variability in northwestern TP glaciers, whereas ablation-season air temperatures primarily regulate mass balance in southeastern regions (Zhu et al., 2018, 2020, 2021). Monsoon-driven cloud cover significantly influences summer surface energy budgets, as evidenced by detailed observations at East Rongbuk Glacier on the northern slopes of Mount Everest (Liu et al., 2021). These findings collectively demonstrate pronounced spatial heterogeneity in the sensitivity of TP glaciers to climate forcing. However, understanding the mechanisms underlying extreme mass loss events across TP and adjacent regions remains inadequate.

Emerging evidence identifies compound heat-drought events as primary drivers of extreme glacier mass loss. Regional case studies across cryosphere hotspots—including the eastern Tien Shan (Xu et al., 2024), Qilian Mountains (Chen et al., 2024), and Tanggula and Nyainqêntanglha ranges (Zhu et al., 2024b)—reveal

https://doi.org/10.5194/egusphere-2025-2579
Preprint. Discussion started: 31 July 2025

unprecedented mass loss rates associated with atmospheric teleconnections and glacier surface energy budget anomalies. These events typically result from synergistic interactions between external forcing (heat extremes/precipitation deficits) and intrinsic glacier responses (albedo feedbacks/turbulent heat flux anomalies). When superimposed, these drivers can push glacier systems beyond equilibrium thresholds within weeks, producing nonlinear mass losses that challenge conventional model predictions. However, comprehensive event attribution remains challenging across most of TP.

This knowledge gap stems from two critical limitations: (1) methodological constraints in detecting extremes from short mass balance records (under ten years), and (2) sparse in situ monitoring networks—fewer than ten TP glaciers have decadal-scale measurements. Traditional extreme detection methods (e.g., 10th percentile thresholds, generalized extreme value [GEV] distributions) require multi-decadal data unavailable for over 90% of TP glaciers. Consequently, developing robust frameworks for identifying extremes in short-term observations (under ten years) is essential for the region.

The exceptional 2022 heatwave, characterized by unprecedented air temperature anomalies and precipitation deficits, served as an ideal natural experiment to address these challenges. Researchers have systematically analyzed the temporal characteristics (frequency/duration), intensity metrics, and hydrological impacts of the 2022 heatwave-drought events in both the Yangtze River Basin (Hua et al., 2023; Jeong et al., 2023) and TP (Yan et al., 2024; Zhou et al., 2024). Hua et al. (2023) demonstrated that a 6.45 °C temperature anomaly in central China broke historical records and reshaped climatological baselines for extreme temperature projections. During summer 2022, central-eastern TP recorded mean maximum air temperatures 3.5 °C above the 1961–2013 baseline (Zhou et al., 2024). Concurrently, central-eastern TP precipitation was 2.4 σ below the 1961–2013 mean (Zhou et al., 2024), while southern China experienced rainfall deficits of 2–3 mm·day^{-1} (Jeong et al., 2023). Multiple drivers have been identified, including synoptic-scale circulation

https://doi.org/10.5194/egusphere-2025-2579
Preprint. Discussion started: 31 July 2025

anomalies (Hua et al., 2023; Duan et al., 2024), Indian Ocean Dipole–La Niña interactions (Jeong et al., 2023), land-atmosphere feedbacks (Li et al., 2023), and localized energy budget perturbations (Tian et al., 2023; Zhang et al., 2023b). These studies collectively reveal that both TP and eastern China faced unprecedented extreme heat and precipitation deficits during summer 2022.

The key glaciated complexes most exposed to this extreme event—located in the Central Tanggula Mountains (encompassing the Geladandong and Dongkemadi regions, and Puruogangri Ice Cap), a critical cryospheric zone in central TP—provide a unique opportunity to develop novel methodologies for identifying extreme mass loss events and elucidating their driving mechanisms. Continuous mass balance monitoring began in 1989 at Xiao Dongkemadi Glacier in the Dongkemadi region (Pu et al., 2008; Yao et al., 2012). Since entering a negative mass balance regime around 1995, Xiao Dongkemadi Glacier has experienced accelerated mass loss at ~−0.3 m w.e. yr^{-1} since 2000 (Pu et al., 2008; Yao et al., 2012; Kang et al., 2015). Research demonstrates that summer mass balance controls annual mass balance variations in summer-accumulation-type glaciers in the Dongkemadi region (Liang et al., 2018). The Geladandong region recorded glacier mass loss rates of -0.24 ± 0.08 m w.e. yr^{-1} from the 1960s to 2018 (King et al., 2023). Sangqu Glacier, located south of Geladandong, was selected for in situ glacio-meteorological observations. Meltwater from Sangqu Glacier drains into Siling Co, the largest lake in Tibet. Therefore, investigating extreme mass loss events in this region will improve the understanding of glacier change patterns and support sustainable water resource management.

Hence, this study aims to (i) investigate the energy-mass balance characteristics of Sangqu Glacier in the Geladandong region; (ii) develop a novel framework for detecting extreme mass loss events in short-term glacier mass balance records; and (iii) elucidate melting mechanisms driven by the unprecedented 2022 summer heatwaves. By integrating multi-source observational data with a surface energy-mass balance model, this work advances understanding of glacier responses to extreme heatwaves and proposes an innovative thermal-threshold framework—a

https://doi.org/10.5194/egusphere-2025-2579
Preprint. Discussion started: 31 July 2025

methodological advancement addressing critical gaps in TP cryosphere research.

2. Study Area

The valley-type continental Sangqu Glacier (33.1951°N, 91.1362°E) in Geladandong was selected as the study site (Figure. 1). This south-facing glacier has a length of 2.2 km and covers 18 km². Spanning an elevational range of 5,400–6,104 m a.s.l., its equilibrium line altitude (ELA) is ~5,700 m a.s.l. (Guo et al., 2015). Situated in central TP, the region experiences low air temperatures and a semi-arid continental climate. Over 70% of annual precipitation occurs during June–September, coinciding with the warmest season (Zhu et al., 2024a). Glacier ablation and accumulation in Geladandong primarily occur from June to September, characterized by a short melt season (Pu et al., 2008). Multi-temporal digital elevation model (DEM) differencing and in situ stake measurements reveal continuous mass loss in this region since the 1990s (Yao et al., 2012; King et al., 2023). Moreover, Sangqu Glacier lies at the northern limit of Indian monsoon influence (Tian et al., 2001; Yao et al., 2013).

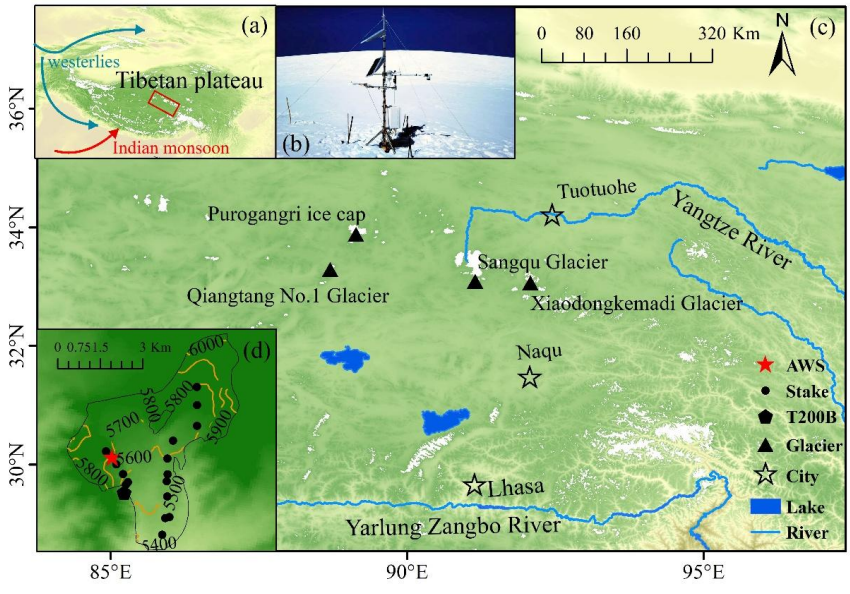

Figure 1. Overview of the study area. (a) and (c) Location of the study area on TP. (b) Photos of AWS on Sangqu Glacier (Photo credit: Fei Zhu). (d) Stakes in October 2019, automatic weather stations, and precipitation gauges are located on Sangqu Glacier.

https://doi.org/10.5194/egusphere-2025-2579
Preprint. Discussion started: 31 July 2025

3. Data

3.1 Meteorological Data on Glacier Surface

An automatic weather station (AWS) was installed on Sangqu Glacier at 5,700 m a.s.l. in October 2020 (Figure. 1b and 1d). Hourly measurements included air temperature, relative humidity, wind speed, incoming/outgoing shortwave radiation, and incoming/outgoing longwave radiation. Air temperature and relative humidity probes, along with wind speed, were mounted 2 m above the glacier surface. Radiation sensors were installed greater than 1.6 m above the surface. Data from July 2021 were incomplete due to power failure; operations resumed on 13 July 2021. A Geonor T-200B precipitation gauge on adjacent bedrock (5,665 m a.s.l.) recorded precipitation at 30-min intervals (Figure. 1d). Meteorological data cover the period October 2020 to July 2022.

3.2 Glacier Mass Balance Data

Glacier mass balance measurements began in October 2019 using stake and snow-pit methods. Stakes were distributed between 5,400 and 5,750 m a.s.l.. Stake heights and snow-pit characteristics were measured in October 2019, October 2020, October 2021, and July 2022. Using these measurements and assumed densities (snow: 300 kg m^{-3}; ice: 900 kg m^{-3}), mass balance data were derived for three periods: October 2019–October 2020, October 2020–October 2021, and October 2021–July 2022. Point and glacier-wide mass balances were calculated following Yao et al. (2012).

3.3 Other Data

Hourly ERA5 reanalysis data (Hoffmann et al., 2019) including air temperature, precipitation, relative humidity, wind speed, and incoming shortwave radiation were used. These data reconstructed meteorological conditions at the AWS locations. Glacier boundaries were obtained from the Second Chinese Glacier Inventory (Guo et al., 2015). The 90-m resolution Shuttle Radar Topography Mission (SRTM) digital elevation model (DEM) was used to extract elevation, slope, and aspect. These data also drove model calculations of top-of-atmosphere radiation (Hock and Holmgren,

https://doi.org/10.5194/egusphere-2025-2579
Preprint. Discussion started: 31 July 2025

2005).

4. Methods

4.1 Energy and Mass Balance Model

We established the distributed coupled energy balance–snow/firn model (EBFM) and subsurface model for Sangqu Glacier. This model describes the evolution of vertical temperature, density, and water content profiles within the snow/ice pack, incorporating percolation and refreezing processes (Van Pelt et al., 2012). The EBFM has been successfully applied to mountain glaciers, including Abramov Glacier in the Pamir Alay (Kronenberg et al., 2022) and Kuoqionggangri Glacier in the Nyainqêntanglha Mountains (Zhu et al., 2024b). Detailed model descriptions are provided by Van Pelt et al. (2012, 2019). The sum of each surface energy component is equal to the melt energy (Q_M) and the surface energy balance formula is as follows (Van Pelt et al., 2012):

$$Q_M = S_{net} + l_{net} + Q_H + Q_L + Q_G \quad (1)$$

where S_{net} is the net shortwave radiation, which consists of the incoming (S_{in}) and outgoing (S_{out}) shortwave radiation. The S_{out} depends on the albedo of the glacier surface. L_{net} is the difference between the incoming (L_{in}) and the outgoing longwave radiation (L_{out}), where Q_H and Q_L are the sensible and latent heat fluxes, respectively. Q_G represents the snow and ice heat flux. Following micrometeorological convention, energy fluxes directed towards the surface are positive. The dichotomous iterative method was used to calculate the glacier surface temperature, and the surface temperature was constrained at less than 0°C.

The glacier mass balance on TP comprises four primary processes: snowfall, melting, sublimation/evaporation, and refreezing at the glacial surface. The surface mass balance components at each grid point can be expressed as:

$$B = P - M - E_{eva/sub} + C_{rf} \quad (2)$$

where B denotes the point mass balance of each grid. P is for precipitation. M is the amount of melt on glacier surface. $E_{eva/sub}$ refers to the sublimation and

https://doi.org/10.5194/egusphere-2025-2579
Preprint. Discussion started: 31 July 2025

evaporation. C_{rf} is for refreezing. Surface ablation involves melting, sublimation and evaporation. In this study, sublimation and evaporation were quantified based on latent heat flux and surface temperature. Specifically, the phase transition criteria were defined as follows: sublimation was identified under conditions where surface temperatures remained below the melting point while latent heat flux exhibited negative values. Conversely, evaporation was classified when surface temperatures exceeded the melting point with concurrent negative latent heat flux values. Additionally, the model explicitly includes deposition and condensation processes, which are strictly governed by positive latent heat flux conditions. Here, deposition occurs when surface temperatures remain below the melting point with positive latent heat flux, while condensation occurs when surface temperatures exceed the melting point with positive latent heat flux. However, both processes were excluded from the final analysis due to their negligible impact on the overall mass balance. Mass accumulation comprises snowfall and refreezing processes. Specifically, surface accumulation was derived from solid precipitation events, determined by a temperature-dependent rain-snow transition threshold applied to atmospheric forcing data. Subsurface liquid water sources—including meltwater, rainfall, and condensation—were tracked as potential contributors to refreezing events.

In this study, the EBFM was driven by air temperature, relative humidity, wind speed, total precipitation, and cloud fraction at hourly intervals from October 2019 to September 2022. To obtain the air temperature, relative humidity, wind speed, total precipitation, and cloud fraction at hourly intervals from October 2019 to October 2021 and August 2022 to September 2022, meteorological data were reconstructed at hourly intervals using the random forest method by combining the air temperature, relative humidity, wind speed, and incoming shortwave radiation measured at AWS and ERA5. Cross-validation techniques were also employed for the correction of ERA5 data. Specifically, a 3-fold cross-validation approach was implemented for modeling relative humidity and wind speed. In contrast, for air temperature and S_{in}, our tests indicated that a 10-fold cross-validation method was more suitable. The

https://doi.org/10.5194/egusphere-2025-2579
Preprint. Discussion started: 31 July 2025

correlation coefficients (R) were used to evaluate the simulation results. The R for air temperature, relative humidity, wind speed, and incoming shortwave radiation were 0.99, 0.88, 0.92, and 0.87 for the measurements and simulations on a daily scale (Figure. A1). The cloud fraction was defined as the ratio of incoming shortwave radiation to total radiation at the top of the atmosphere. The hourly calculation of S_{TOA} (total radiation from the top of the atmosphere) was based on elevation, slope, and aspect parameters (Hock & Holmgren, 2005). The glacier-wide mass balance was calculated using the cloudiness calculation method of Favier et al. (2004). Comparison with the (S_{in}/S_{TOA}) calculation gives a root mean square error (RMSE) of 139.89 mm w.e., a coefficient of determination (R^2) of 0.71 and a percentage bias (PBIAS) of 18.4%. We also estimated the total precipitation on Sangqu Glacier from October 2019 to September 2022. This was achieved by combining total precipitation data from ERA5 with data from direct measurements. First, we calculated the ratio (0.54) of total measured precipitation to that estimated by ERA5 for the overlap period (October 2020 to July 2022). Then, the ratio was used to correct all reanalysis precipitation data from October 2019 to September 2021. This approach has been extensively utilized in glacier–related studies on TP (Yang et al., 2013; Potocki et al., 2022; Zhu et al., 2024a).

The spatial interpolation of meteorological data considered the topographic conditions (elevation, slope, and aspect) of Sangqu Glacier. The mean air temperature lapse rate was 0.65°C/100 m. Precipitation gradient was the parameter for the EBFM model, taking into account glacier mass balance and albedo. The wind speed and relative humidity measured at the AWS represented the entire glacier. The methodology for calculating the energy balance components at the glacier surface was based on the findings of previous studies. The S_{in} was simulated as described by Klok & Oerlemans (2002) and Van Pelt et al. (2012) and accounts for the grid aspect and shading by the surrounding terrain. S_{out} depends on surface albedo. Snow albedo was related to temperature and humidity (Oerlemans and Knap, 1998; Bougamont et al., 2005; Van Pelt et al., 2019), and ice albedo was calculated using the dew point

https://doi.org/10.5194/egusphere-2025-2579
Preprint. Discussion started: 31 July 2025

temperature (Mölg et al. (2008). The L_{in} was calculated based on the relative humidity and air temperature (Brunt, 1932). L_{out} was calculated using the Stefan–Boltzmann law. Q_H and Q_L were calculated using the method proposed by Klok & Oerlemans (2002). Q_G was obtained as the sum of the conductive heat fluxes (Reijmer & Hock, 2008; Van Pelt et al., 2012).

The interpolation of meteorological data at the glacier scale, as well as the area-averaged energy and mass balance, are related to the surface elevation of glaciers. Beckmann et al. (2023) found the surface elevation feedback largely amplifies melting for scenarios with and without extremes, with additional mass loss attributed to this feedback having the greatest impact on projected sea level. In this study, we employ sensitivity analysis to examine the extent to which the mass balance of the Sangqu Glacier responds to variations in surface elevation. With SRTM data serving as the benchmark for surface elevation, we established ten experimental scenarios encompassing changes of +2 m, +5 m, +10 m, +20 m, and +50 m (alongside corresponding decreases of –2 m, –5 m, –10 m, –20m, and –50 m). Throughout these experiments, parameters related to air temperature, total precipitation, and albedo were held constant while the model was executed. The sensitivity analysis reveals that, when considering the scenarios with positive changes (+2m to +50m), the magnitude of the mass balance response to surface elevation variations on Sangqu Glacier amounts to 9.4 mm w.e. m^{-1}. In contrast, for the scenarios with negative changes (–2 m to –50 m), the magnitude of the response increases to 12.6 mm w.e. m^{-1}. The terrain-associated feedback mechanism has the potential to exacerbate glacier mass loss on TP when faced with decreasing glacier surface elevation.

The standardized heatwave index (S_{HI}) was employed to detect heatwave events (Raei et al., 2018; Shan et al., 2024). This index quantifies temperature deviations relative to 30-year climatological norms. It ranks heatwaves by their recurrence probability within a dynamic reference period. The reference period and climate normal for calculating such probabilities must be carefully chosen because of the non-stationarity of temperature records caused by global warming. Following Shan et al.

https://doi.org/10.5194/egusphere-2025-2579
Preprint. Discussion started: 31 July 2025

(2024), we implemented a 30-year moving window to address non-stationarity. Therefore, we used the past 30 years as the historical reference period and averaged the daily values. The S_{HI} was calculated for each day as follows (Raei et al., 2018; Shan et al., 2024):

$$\overset{\Lambda}{T}_{m,j} = \begin{cases} \frac{1}{N_h} \sum_{j=i-N_h+1}^{i} T_{m,j} & if \geqslant N_h \\ \frac{1}{N_h} \left(\sum_{j=365-N_h+i+1}^{365} T_m - 1, j + \sum_{j=1}^{i} T_{m,j} \right) & if < N_h \end{cases} \quad (3)$$

$$S_{HI}^{m,j} = \Phi^{-1}\left(F_{m,j}^{h}\left(\overset{\Lambda}{T}_{m,j}\right)\right) \quad (4)$$

where i and j represent calendar days. M is the number of years of historical observations, and $T_{m,j}(℃)$ is the daily mean temperature at day i of year M. N_h is the length of the accumulation period for a heatwave; $\overset{\Lambda}{T}_{m,j}$ is the mean temperature over the accumulation period up to and including day i. $F_{m,j}^{h}$ is the cumulative distribution function (CDF). Φ^{-1} is an inverse standard normal CDF. In this study, we calculated the average between February 28 and 29, subsequently removed the leap day (February 29) to maintain a 365-day annual cycle. We set up a 3-day averaging window to run the S_{HI} program and used S_{HI} value greater than 1 to identify heat waves.

4.2 Modelling Validation and Uncertainty

Model validation utilized in situ measurements of albedo, S_{in}, L_{in}, and L_{out} from AWS to evaluate EBFM performance. The point mass balance at different elevations on the glacier surface and glacier–wide mass balance measured during October 2019–October 2020, October 2020–October 2021, and October 2021–July 2022 was used to assess the accuracy of the EBFM model simulations.

Figure. 2 shows the results of comparing the measured and modelled albedo, S_{in}, L_{in}, and L_{out} at the AWS sites. The measured and modelled albedo show good agreement, with RMSE and R of 0.1 and 0.68 at daily scale, respectively (Figure. 2a).

https://doi.org/10.5194/egusphere-2025-2579
Preprint. Discussion started: 31 July 2025

The RMSE and R for weekly scale observations and modelled albedo are 0.09 and 0.76, respectively (Figure. S1). Observed and modelled albedos during extreme heat waves (30 May to 9 June and 3 July to 16 July) were also compared, with RMSE and R of 0.14 and 0.77, respectively. The measured and modelled R and RMSE of S_{in} were 0.9 and 32.4 W m^{-2}, respectively (Figure. 2b). Discrepancies between observed and simulated S_{in} were mainly due to errors in the estimated cloud fraction (Van Pelt et al., 2012). Good agreement between the measured and modelled albedo and S_{in} ensures the accuracy of S_{net}, which is the main energy source at the glacier surface. The L_{in} R and RMSE of the measured and modelled are 0.88 and 26.2 W m^{-2}, respectively (Figure. 2c). The L_{out} R and RMSE of the measured and modelled are 0.95 and 10.6 W m^{-2}, respectively (Figure. 2d). This good agreement ensures the accuracy of the net longwave and surface temperature simulations of the surface energy balance.

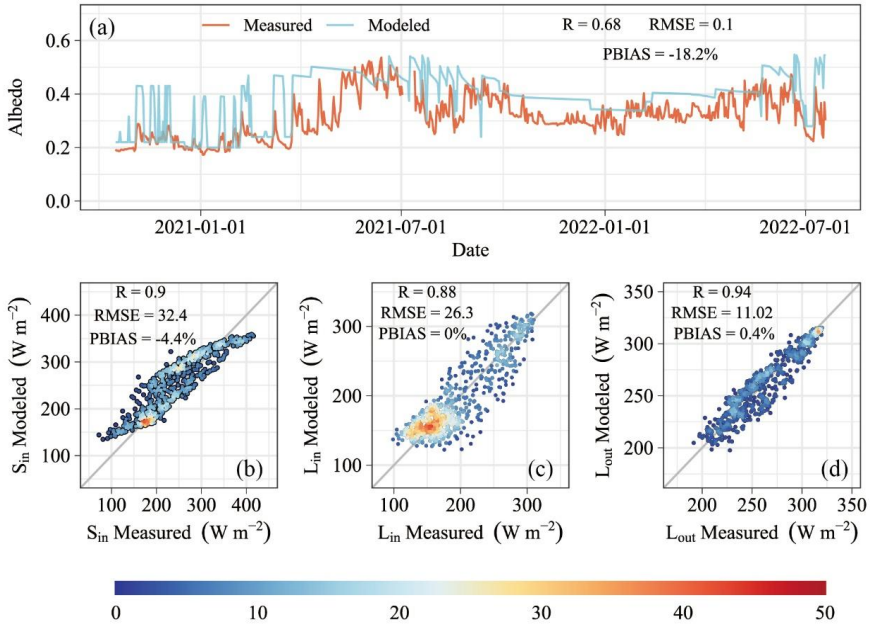

Figure 2. Comparison of (a) albedo in daily scale, (b) S_{in}, (c) L_{in}, and (d) L_{out}, measured and modelled at the AWS sites on Sangqu Glacier.

We also compared the measured and modelled mass balances. The RMSE of the measured and modelled point mass balances was 297 mm w.e. (Figure. 3a). The

https://doi.org/10.5194/egusphere-2025-2579
Preprint. Discussion started: 31 July 2025

RMSE of the measured and modelled glacier–wide mass balance was 211 mm w.e. (Figure. 3b). We also present comparisons between observations and model simulations for the periods October 2019–October 2020, October 2020–October 2021, and October 2021–July 2022 (Figure. 3c, d, and e). RMSE values between simulated and observed results were 322, 256, and 293 mm w.e., respectively. This consistency allowed us to analyze the seasonal and interannual characteristics of the surface energy and mass balance of Sangqu Glacier.

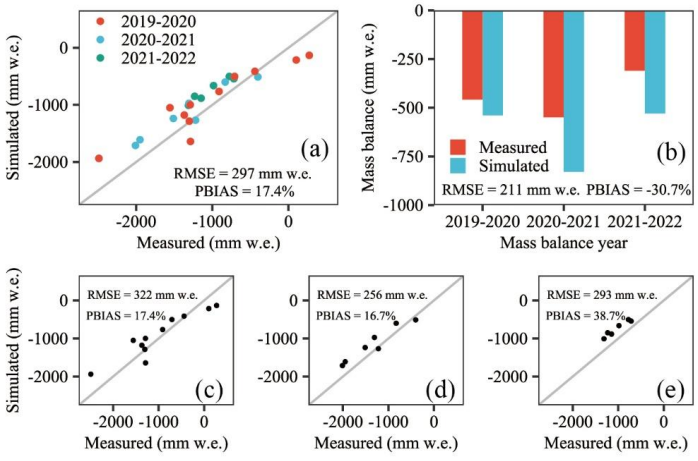

Figure. 3. Comparison of measured and modelled mass balance at (a) point scale and (b) glacier–wide scale. (c), (d) and (e) are point scale comparisons of the mass balance measurements and modelling for the years 2019-2020, 2020-2021 and 2021-2022 respectively. 2019–2020 refers to October 2019 to October 2020 and also 2020–2021. 2021–2022 refers to October 2021 through July 2022.

The uncertainty in model outputs arises primarily from key parameters governing albedo (snow, firn, and ice), precipitation gradients, critical temperature thresholds, and turbulent flux calculations, all of which critically determine mass balance simulation accuracy. Following standard sensitivity analysis protocols in glaciology, we implement a ±10% parameter perturbation approach, a methodology ubiquitously adopted in both degree-day and energy-mass balance modeling frameworks for systematic uncertainty quantification. Snow albedo and firn albedo (±0.03) uncertainties were used as recommended by Van Pelt et al. (2012). The total uncertainty for the modelled mass balance in each year was estimated using the error

https://doi.org/10.5194/egusphere-2025-2579
Preprint. Discussion started: 31 July 2025

propagation law described by Zhu et al. (2024b) and Zhu et al. (2021). The uncertainty in the mass balance averaged over three years was 222.9 mm w.e. (Table S2, S3, and S4). The uncertainty of the melt during extreme heat waves has also been discussed and was found to be 150.2 mm w.e. (Table S1).

4.3 A Dual-Threshold Framework for Identifying Extreme Mass Loss Events in Short-Term Glacier Mass Balance Records

Accurately identifying extreme mass balance events across different temporal scales is crucial for advancing our understanding of the characteristics and mechanisms underlying glacier mass balance responses to climate change. Although conventional approaches such as percentile thresholds (Vargo et al., 2020) (e.g., 10th percentile) and generalized extreme value (GEV) distributions (Thibert et al., 2018) have been widely employed to detect extreme mass loss and melt events, these methods require long-term mass balance records exceeding 30 years. On TP, only Xiao dongkemadi Glacier possesses a continuous observational mass balance series longer than three decades, with monitoring initiated in 1989 (Yao et al., 2012). Most other reported glacier mass balance records in this region typically span less than 10 years. To address this limitation, we compiled available observed and reconstructed annual mass balance data across TP and developed a novel methodology capable of reliably identifying extreme mass loss events from short-term records (under 10 years).

This study proposes a dual-threshold extreme event detection method based on quantile-statistical distribution coupling. The mathematical framework is constructed as follows: First, the glacier mass balance (m_b) time series is partitioned into training and test sets, where the training data is denoted as $\{m_{b,i}\}_{i=1}^{n}$ with corresponding years $\{y_i\}_{i=1}^{n}$. The baseline criterion for extreme events is defined using the p-quantile threshold of the training set:

$$Q_p = Inf\{m_b \in R | F_n(m_b) \geq p\} \quad (5)$$

Where Q_p denotes the p - quantile threshold for extreme event identification.

https://doi.org/10.5194/egusphere-2025-2579
Preprint. Discussion started: 31 July 2025

$F_n(m_b)$ corresponds to the empirical cumulative distribution function of the training set mass balance data. $p \in (0,1)$ defines the target probability level (default $p = 0.1$) for extreme event selection.

To establish the statistical distribution criterion, we calculate the training set parameters:

$$\mu = \frac{1}{n}\sum_{i=1}^{n} m_{b,i} \tag{6}$$

$$\sigma = \sqrt{\frac{1}{n-1}\sum_{i=1}^{n}\left(m_{b,i} - \mu\right)^2} \tag{7}$$

Where μ represents the mean of training set mass balance values. σ quantifies the standard deviation of training set mass balance values. n indicates the total number of training years. $m_{b,i}$ refers to the mass balance measurement in the i training year.

A parameter space traversal algorithm is employed to solve for the statistical threshold parameter kk that satisfies the equivalence conditions:

$$\begin{cases} \mu - K\sigma \leqslant Q_p \\ \{y_i | m_{b,i} < \mu - K\sigma\} \equiv \gamma_T \end{cases} \tag{8}$$

Where K controls the multiplier of standard deviations from the mean. $\mu - K\sigma$ specifies a candidate statistical threshold constrained by the quantile boundary Q_p. γ_T comprises years identified as extreme events through the quantile criterion.

Let the solution set be $K \in [K_{\min}, K_{\max}]$, we then construct dual detection thresholds:

$$\begin{aligned} T_{strict} &= \mu - K_{\max}\sigma \ \ (strict\ threshold) \\ T_{relaxed} &= \mu - K_{\min}\sigma \ \ (relaxed\ threshold) \end{aligned} \tag{9}$$

where $K_{\max}$ and $K_{\min}$ define the maximum and minimum valid scaling coefficients satisfying the equivalence conditions, while T_{strict} and $T_{relaxed}$ delimit the strict and

https://doi.org/10.5194/egusphere-2025-2579
Preprint. Discussion started: 31 July 2025

relaxed thresholds that respectively ensure full consistency with historical extremes and complete coverage of quantile-defined events. During testing, a year y_i is classified as an extreme event if $m_{b,i} < T_{relaxed}$, while $m_{b,i} < T_{strict}$ indicates a high-confidence extreme event.

This method achieves mathematical equivalence between quantile-based and statistical-distribution criteria through feasible region solving of parameter K. The dual-threshold design effectively quantifies uncertainty boundaries in detection results, maintaining consistency with historical extreme event definitions while enhancing model adaptability to distribution characteristics.

5. Results

5.1 Seasonal Cycle and Interannual Variation of Energy and Mass Balance

Seasonally varying glacier–wide energy balances and their components are shown in Figure. 4a. The S_{net} shows significant seasonal variability in the range of 40 W m^{-2} to 66.3 W m^{-2}, and this variability is mainly driven by the seasonal shift in the solar elevation angle in conjunction with the glacier surface albedo. L_{net} is the major energy-loss term for the glacier surface energy balance (Figure. 4a). The maximum and minimum values of net longwave radiation are −16.2 W m^{-2} and −82.3 W m^{-2}, which occur in August and March, respectively. The mean L_{net} in the warm and cool seasons are −31 W m^{-2} and −77.2 W m^{-2}, respectively. The difference in L_{net} between the warm and cool seasons mainly depends on the difference between L_{in} and L_{out}. In this study, L_{in} is influenced by both air temperature and relative humidity, both of which reach high values in the warm season, corresponding to higher L_{in}. The L_{out} calculated from the glacier surface temperature was also high during the warm season. Combining L_{in} and L_{out}, the absolute value of L_{net} was found to be lower during the warm season than during the cold season.

The Q_H on Sangqu Glacier were continuously above 0 W m^{-2} and was an important heat source in the energy balance (Figure. 4a). This indicates that the atmosphere continuously supplies heat to the glacier surface, which helps maintain the

https://doi.org/10.5194/egusphere-2025-2579
Preprint. Discussion started: 31 July 2025

glacier surface temperature. The Q_H in the cold and warm seasons are 39.3 W m^{-2} and 21.5 W m^{-2}, respectively, and this difference may be closely related to the temperature gradient between the glacier surface and the atmosphere, as well as seasonal changes in wind speed. In contrast, the Q_L on Sangqu Glacier is usually less than 0 W m^{-2}, and the mean Q_L is −10.7 W m^{-2}, indicating that sublimation or evaporation processes are continuously occurring at the glacier surface (Figure. 4a).

Q_G depends on the heat transfer coefficients of ice and snow, as well as the temperature gradient (the temperature difference between the surface and the interior of the glacier). The mean Q_G is 1 W m^{-2}, indicating that the Q_G accelerates the melting process at the glacier surface (Figure. 4a). Further analysis showed that Q_G in the cold season played an important role in maintaining the energy balance of the glacier surface, whereas in the warm season, it accelerated the melting of the glacier surface. Combining the S_{net}, L_{net}, Q_H, Q_L, and Q_G, it was found that the melt energy started to be higher than 0 W m^{-2} in May, indicating that the melt on Sangqu Glacier started, with peaks in July and August (Figure. 4a).

The glacial mass balance and its components at the glacial scale are shown in Figure. 4b. Melt, snowfall, refreezing, and sublimation/evaporation are the major mass components of glaciers on the central TP. Mass replenishment comes from snowfall and the refreezing of the snowpack. 73.2% of snowfall is concentrated in the warm season, and most precipitation falls as snow on glacier surfaces during the warm season. Cold–season snowfall accounts for only 27% of the total snowfall, with less mass replenishment. The total snowfall in April and May, which affects warm–season albedo and glacier melt rates, accounted for 13.3% of the total snowfall. Meltwater on the glacier surface and water content in the snow are the main sources of mass for refreezing. The volume of refreezing peaks in June, which is related to snow cover and meltwater on the glacier surface. During the observation period, the refreezing amount on Sangqu Glacier accounted for 4% of the melting amount.

The major mass losses from glaciers include melt, sublimation and evaporation. The melt is the dominant component of the mass balance. Melting begins at the

https://doi.org/10.5194/egusphere-2025-2579
Preprint. Discussion started: 31 July 2025

glacier surface in May and peaks in July or August, which is related to the seasonal distribution of melt energy. 85% of melt occurs during the warm season. June, July, August, and September account for 18%, 25%, 34%, and 9% of the total melt, respectively.

Sublimation/evaporation is a component of the mass balance that cannot be ignored; in this study, sublimation/evaporation on the Sangqu Glacier accounted for 17% of the mass balance. Previous studies have shown that Sublimation and evaporation of the glacier surface, as a mass loss term, varies spatially on TP (Zhu et al., 2020; Guo et al., 2022). Sublimation and evaporation on Sangqu Glacier (−161 mm w.e. yr^{-1}) was similar to Zhadang Glacier (−154.4 mm w.e. yr^{-1}) (Zhu et al., 2018) and Qiangtang No. 1 Glacier (−175.5 mm w.e. yr^{-1}) (Li et al., 2018), lower than Guliya (−194 mm w.e. yr^{-1}) (Zhu et al., 2022b) and Muztag Ata No. 15 Glacier (−272 mm w.e. yr^{-1}) , higher than Parlung No. 4 (−144.8 mm w.e. yr^{-1}) and Parlung No. 94 Glacier (−60 mm w.e. yr^{-1}) (Yang et al., 2013; Zhu et al., 2018). Differences in sublimation and evaporation from glaciers indicate differences in the exchange of water and heat between the glacier surface and the atmosphere in different climatic zones (Zhu et al., 2020; Guo et al., 2022).

https://doi.org/10.5194/egusphere-2025-2579
Preprint. Discussion started: 31 July 2025

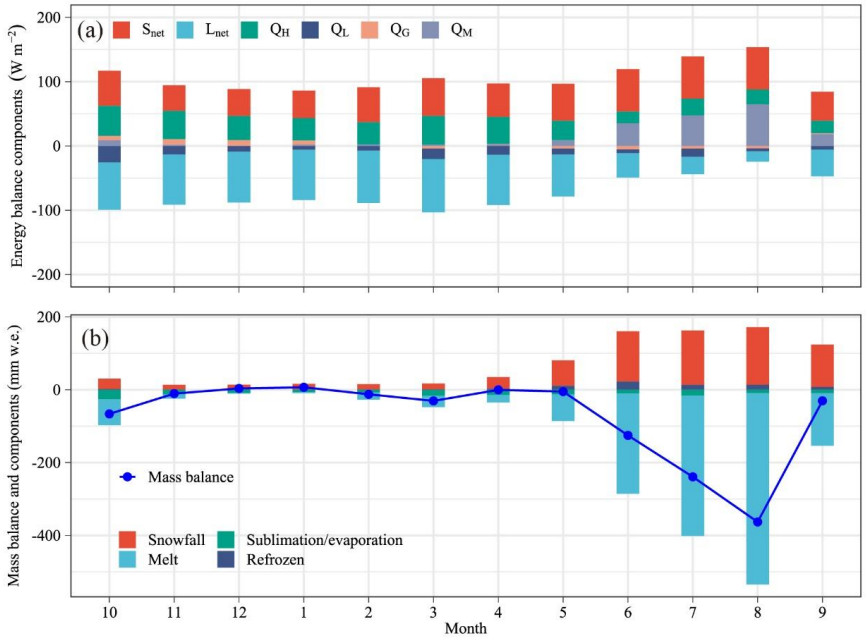

Figure 4. (a) Glacier–wide mean monthly energy and (b) mass fluxes of the energy and mass balance components from October to September during 2019-2022.

The interannual variability of the mass balance and its components was examined. Figure. 5 quantifies glacier-wide fluctuations in mass balance, snowfall, melt, sublimation/evaporation, and refreezing. The 2021-2022 mass balance year emerged as historically exceptional, recording –1 251 mm w.e. - corresponding to 2.3-fold larger magnitude than 2019-2020 (–540 mm w.e.) and 1.5 times that of 2020-2021 (–831 mm w.e.) - representing the most severe deficit since observational records began.

In the central TP, sublimation/evaporation and refreezing typically constitute a small portion of the mass balance, while snowfall and melting account for a larger proportion. The melt exhibits significant interannual variability, ranging from 1464.2 mm w.e. in 2019–2020 to 1736.9 mm w.e. in 2021–2022. Snowfall variability was comparable to sublimation/evaporation, with changes of 307 mm w.e. and 70.6 mm w.e. from 2019–2020 to 2021–2022, respectively. Refreezing shows the smallest variability, ranging from 20.9 mm w.e. to 60.5 mm w.e.. Thus, the interannual variability in the mass balance of Sangqu Glacier was primarily influenced by melting

https://doi.org/10.5194/egusphere-2025-2579
Preprint. Discussion started: 31 July 2025

and snowfall during the study period.

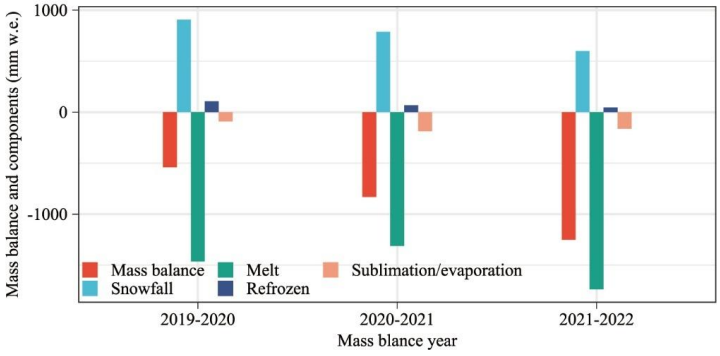

Figure 5. Interannual variation in glacier–wide mass balance and its components on Sangqu Glacier in 2019–2020, 2020–2021, and 2021–2022.

5.2 Extreme mass loss and melting event detection

5.2.1 Identification and Validation of Extreme Glacier Mass Loss Events on TP

The observed and reconstructed annual mass balance records across TP enable the application of this novel methodology to define critical thresholds for extreme mass loss events. To validate the methodology, we compiled annual mass balance data from five glaciers: Xiao dongkemadi Glacier, Qiyi Glacier, Guliya Glacier, Ningchan No. 1 Glacier, and Anglong Glacier. The derived relaxed and strict thresholds are 1.06 and 1.13 for Xiao dongkemadi Glacier (Figure. 6a), 1.28 and 1.34 for Qiyi Glacier (Figure. 6b), and 1.29 and 1.34 for Guliya Glacier (Figure. 6c), respectively. For Ningchan No. 1 Glacier (Figure. S4a) and Anglong Glacier (Figure. S4b), the relaxed thresholds are 1.28 and 1.35, while the strict thresholds are 1.49 and 1.60, respectively. Using this method, we identified 4, 4, and 6 extreme mass loss events in Xiao dongkemadi Glacier (Figure. 6a), Qiyi Glacier (Figure. 6b), and Guliya Glacier (Figure. 6c), respectively. For Ningchan No. 1 Glacier (Figure. S4a) and Anglong Glacier (Figure. S4b), 5 extreme mass loss events were identified in each case.

Since Xiao dongkemadi Glacier shares similar climate characteristics with Sangqu Glacier, we applied its relaxed (1.06) and strict (1.13) thresholds to calculate critical thresholds for Sangqu Glacier. The resulting thresholds were determined as –1,278 mm w.e. (strict) and –1,252 mm w.e. (relaxed). For the 2021/2022 mass balance

https://doi.org/10.5194/egusphere-2025-2579
Preprint. Discussion started: 31 July 2025

year, the calculated value (−1,251 mm w.e.) approached the relaxed threshold (−1,252 mm w.e.) with a 0.08% deviation (Δ=1 mm w.e.), but was 27 mm w.e. less negative than the strict threshold (−1,278 mm w.e.). However, considering the uncertainty bounds (±222.9 mm w.e.), the 2021–2022 mass loss was definitively classified as an extreme event. This conclusion is further supported by two independent datasets: satellite-derived annual averages (2000–2019, Figure. S2) and global 0.5°-resolution glacier mass balance data (1976–2022, Figure. S3), both indicating unprecedented severity. This extreme loss was twice the satellite-derived annual average observed during 2000–2019 (Figure. S2). Furthermore, global 0.5°-resolution glacier mass balance data (1976–2022) indicate that the 2021–2022 values are 600–700 mm w.e. lower than the 1975–2021 mean (Figure. S3).

https://doi.org/10.5194/egusphere-2025-2579
Preprint. Discussion started: 31 July 2025

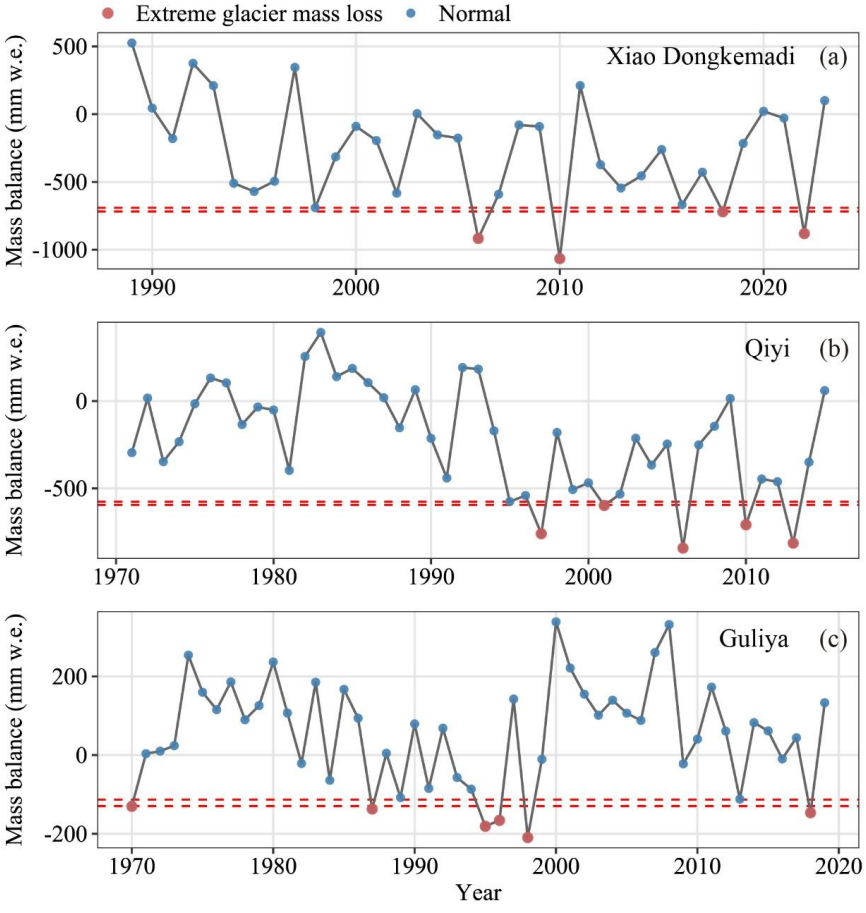

Figure. 6. Annual mass balance time series and extreme mass loss events for (a) Xiao dongkemadi Glacier, (b) Qiyi Glacier, and (c) Guliya Glacier. The data were sourced from Yao et al. (2012), Wei et al. (2025) and Zhu et al. (2022a, 2022b). The red dashed line represents the critical value of k.

5.2.2 Detection and Analysis of Extreme Melting Events in the 2022 Summer on Sangqu Glacier

In Section 5.2.1, we identified the 2021–2022 period as an extreme mass loss year. Building on this finding, we further investigated whether summer melt on Sangqu Glacier reached extreme levels during the 2021–2022 mass balance year.

As presented in Section 5.1, our calculations revealed that the melt magnitude for

https://doi.org/10.5194/egusphere-2025-2579
Preprint. Discussion started: 31 July 2025

the Sangqu Glacier during 2021–2022 (−1,736.91 mm w.e.) was more negative compared to the 2019–2020 (−1,464.17 mm w.e.) and 2020–2021 (−1,311.98 mm w.e.) periods. The strict and relaxed melt thresholds (Xiao dongkemadi) calculated using the methodology in Section 4.3 were −1,747.64 mm w.e. and −1,732.57 mm w.e., respectively. Following our classification criteria (Section 4.3), melt values exceeding either the strict or relaxed threshold are considered extreme. Since the 2021–2022 melt value fell between these thresholds (i.e., less negative than the strict threshold (−1,747.64 mm w.e.) but more negative than the relaxed threshold (−1,732.57 mm w.e.)), it was classified as an extreme melt event.

Air temperature variability is a direct driver of glacier melt, exhibiting a positive correlation with melt intensity. To evaluate whether melt during heatwaves was extreme, we utilized the S_{HI} defined in Section 4.1. The S_{HI}, calculated from long-term daily mean air temperature records (1960–2022) at Tuotuohe National Weather Station, was used to characterize extreme heat events. Based on our criteria ($S_{HI} > 1$ for ≥3 consecutive days), three heatwave periods were identified: 30 May–9 June, 3–16 July, and 3–29 August 2022 (Figure. 7). The associated meteorological anomalies during the heatwave period are shown in Figure 7. The AWS, located at 5,700 m on Sangqu Glacier, exhibited a 2.4 ℃ positive temperature anomaly alongside a 6.5% reduction in relative humidity during the 2022 summer heatwave events, relative to the 2019-2021 (Figure. 7b and 7c). The cloud fraction was reduced by 26 (50%) during the 52 day of extreme heat waves, with an average reduction of 5.4% (Figure. 7d). Precipitation was reduced by an average of 0.3 mm during extreme heat waves (Figure. 7e). Additionally, compared to the 2019–2021 average melt, a 572 mm w.e. increase in mass loss was observed during the 2022 summer heatwaves. Melt during summer heatwaves exhibited significantly higher frequency and intensity than melt during spring heatwaves (Zhu et al., 2024b), with 52 cumulative summer heatwave days producing 1,135 mm w.e. of melt—accounting for 65.2% of the total 2021–2022 melt (Figure. 7f). From this perspective, glacier melt during the heatwave period may be extreme.

https://doi.org/10.5194/egusphere-2025-2579
Preprint. Discussion started: 31 July 2025

To empirically validate this hypothesis, we applied the methodology outlined in Section 4.3. Our analysis conclusively demonstrated that the 2022 summer heatwaves directly triggered melt conditions that surpassed all documented extremes. The strict and relaxed thresholds for extreme melt during this period were −1,134.47 mm w.e. and −1,110 mm w.e., respectively. The total melt during the 2022 summer heatwaves (−1,134.68 mm w.e.) was more negative than the strict threshold (−1,134.47 mm w.e.), confirming its classification as an extreme event.

Our analysis demonstrated that the 2021–2022 annual mass balance, annual melt magnitude, and melt driven by summer heatwaves were all classified as extreme events. These results validate the broad applicability of the methodology proposed in Section 4.3 for detecting extreme mass or melt events across diverse temporal and climatic contexts.

https://doi.org/10.5194/egusphere-2025-2579
Preprint. Discussion started: 31 July 2025

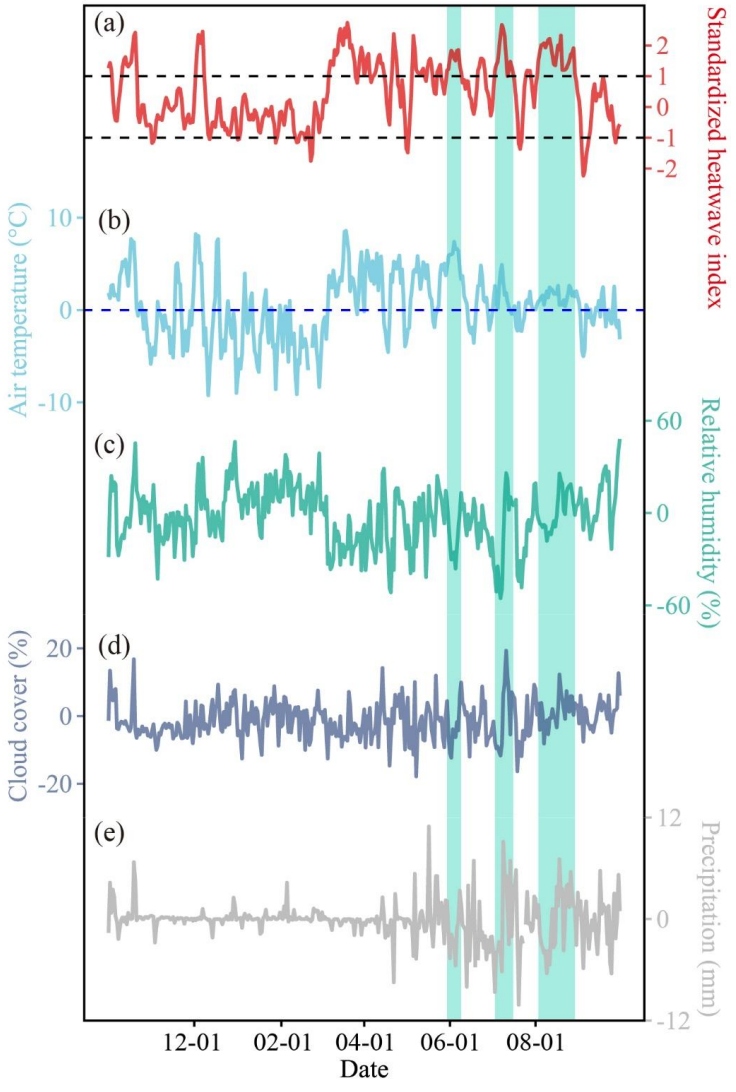

Figure 7. Anomalous meteorological conditions on Sangqu Glacier at 5,700 m during extreme heat waves. (a) standardized heatwave index (S_{HI}). (b) Air temperature (°C), (c) Relative humidity (%), (d) Cloud fraction (%), and (e) Precipitation (mm) anomalies from October 2021 to September 2022 (reference period is October 2019 to September 2021). Color shading represents extreme heat waves.

5.3 Surface Energy Balance Responsible for Extreme Melt during summer 2022 heatwave

The glacier-wide energy balance during heatwave-induced extreme melt events was rigorously analyzed. Our analysis revealed distinct energy balance anomalies in

https://doi.org/10.5194/egusphere-2025-2579
Preprint. Discussion started: 31 July 2025

Sangqu Glacier during extreme heatwaves and melt events, as illustrated in Figure 8 and A2. Compared to the reference period (October 2019-September 2021), the extreme melt period showed a 0.4 W m^{-2} average increase in S_{in} (Figure. 8a) and a 27.9 W m^{-2} decrease in S_{out} (Figure. A2a), collectively enhancing S_{net} by 28.3 W m^{-2} (Figure. A2e). Longwave radiation components exhibited concurrent changes: L_{in} increased by 15.5 W m^{-2} (Figure. 8c) while L_{out} rose by 4.7 W m^{-2} (Figure. A2b), yielding a L_{net} reduction of 10.8 W m^{-2} (Figure. A2f). The combined S_{out} and L_{net} anomalies produced a 17.5 W m^{-2} increase in net radiative flux. Turbulent heat fluxes demonstrated contrasting trends: Q_H increased by 13.5 W m^{-2} (Figure. 8d), whereas Q_L decreased by 7.4 W m^{-2} (Figure. A2c). Q_G showed a 3.3 W m^{-2} reduction (Figure. A2d). These energy budget perturbations - particularly elevated S_{in}, enhanced L_{in}, and amplified Q_H combined with diminished S_{out}, Q_L, and Q_G - significantly increased melt energy availability (Figure. 8e). The observed 10% albedo reduction (Figure. 8b) suppressed surface reflectance, trapping additional shortwave radiation that synergized with enhanced longwave input and Q_H to drive extreme melt during heatwaves.

Current research increasingly identifies energy balance anomalies as the principal driver of extreme glacial melt. Zhu et al. (2024b) demonstrated that early 2022 springtime climatic extremes interacting with anomalous S_{in} and Q_H triggered exceptional melting on Sangqu Glacier. Thibert et al. (2018) reported record melt on Sarennes Glacier (French Alps) controlled by three factors: S_{in} anomalies, Q_L variations, and preseason snowpack conditions. Tian et al. (2023) further established that large-scale circulation patterns modulating cloud cover diurnal cycles induced extreme temperature anomalies in the eastern TP.

Our findings corroborate that energy balance anomalies - characterized by L_{in} enhancement, Q_H amplification, and albedo reduction - primarily drove the 2022 summer heatwave-induced glacier melt. The observed energy partitioning pattern, featuring synergistic radiative-turbulent flux interactions during these summer extreme events, aligns with documented mechanisms in both Alpine and TP glaciers

https://doi.org/10.5194/egusphere-2025-2579
Preprint. Discussion started: 31 July 2025

(Thibert et al., 2018; Zhu et al., 2024b).

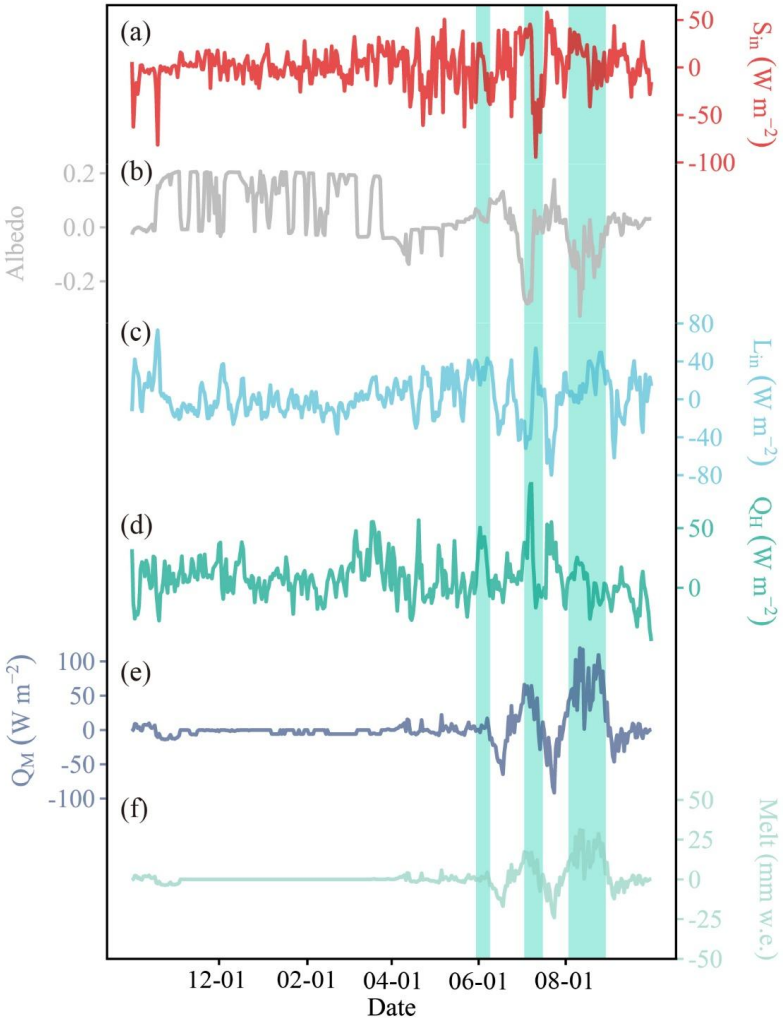

Figure 8. Energy balance components associated with the extreme glacier melt events in glacier-wide scale. Anomalous (a) incoming shortwave radiation, (b) albedo, (c) incoming longwave radiation, (d) sensible heat fluxes, (e) melting energy, and (f) melt from October 2021 to October 2022 (reference period is October 2019–September 2021). Color shading represents extreme heat waves.

6. Discussion

6.1 Effects of Atmospheric Circulation on Extreme Glacier Melt and heat waves

An increasing body of research has demonstrated that large-scale circulation anomalies govern variations in glacier mass balance across TP and adjacent regions

https://doi.org/10.5194/egusphere-2025-2579
Preprint. Discussion started: 31 July 2025

through their modulation of both air temperature and precipitation patterns (Yao et al., 2012). In this study, we provide evidence that atmospheric circulation anomalies constituted the primary driver of the unprecedented glacier melt observed during the 2022 summer heatwave events.

During the initial phase of extreme melting (30 May to 9 June 2022; Figure. 9a and 9d), a vertically stacked anticyclonic anomaly system prevailed over the Sangqu Glacier region. At 200 hPa, the glacier was positioned directly under the core of a TP-centered anticyclonic anomaly. Concurrently at 500 hPa, Mongolian and western Pacific anticyclonic anomalies emerged northeast and east of the glacier, respectively. This multi-level atmospheric configuration generated anomalously intensified easterlies penetrating into the central TP compared to climatological norms. Crucially, the combined effects of these anticyclonic systems - including the northward-displaced SAH and westward-extended WPSH - synergistically induced extreme air temperature anomalies while amplifying glacier melt through enhanced diabatic heating.

The second phase (3-16 July 2022) was characterized by contrasting positional anomalies of the SAH and WPSH relative to climatological baselines (Figure. 9b and 9e). Although anticyclonic anomalies persisted over TP, the SAH exhibited eastward displacement while the WPSH underwent significant westward expansion. This dipole configuration enhanced moisture convergence and intensified subsidence-driven radiative heating over the glacier surface. The synergistic interaction between these atmospheric systems amplified diabatic heating processes, leading to accelerated surface melt rates during this phase.

During the third phase (3-29 August 2022; Figure. 9c and 9f), a vertically stratified anticyclonic anomaly system developed with three-dimensional coherence. At 200 hPa, the anticyclonic anomaly center migrated northeast of Sangqu Glacier, coinciding with an exceptionally eastward-extended SAH spanning from TP to eastern China. Concurrently at 500 hPa, the westward-expanded WPSH stretched from the western Pacific to eastern China and the central TP, establishing a stable anticyclonic

https://doi.org/10.5194/egusphere-2025-2579
Preprint. Discussion started: 31 July 2025

regime east of the glacier. This multi-layered configuration enhanced persistent warm advection thermodynamically while suppressing cloud cover, collectively contributing to the seasonally prolonged and thermally extreme melt episode.

Convergent evidence from recent studies confirms that large-scale circulation anomalies critically drove the 2022 summer heatwaves across TP and eastern China. Previous work has identified that quasi-stationary high-pressure anomalies, combined with anomalous descending motions and enhanced shortwave radiation, were key drivers of both: (1) the extreme summer 2022 heatwave in central China (Hua et al., 2023; Chen & Li, 2023), and (2) the early spring 2022 glacier melt and heatwave in the central TP (Zhu et al., 2024b).

The 2022 summer saw an intensified and westward-extended WPSH coupled with an eastward-extended SAH, which jointly maintained persistent high-pressure anomalies over central-eastern TP (Zhou et al., 2024). Vertical overlap between the WPSH and SAH further reinforced these anomalies, prolonging heatwaves in the region (Li et al., 2021). These circulation patterns corresponded to elevated air temperatures alongside reduced precipitation and cloud cover across central-eastern TP during June-September 2022. The associated descending motions reduced cloudiness, allowing intensified surface shortwave radiation that heated the land (Hua et al., 2023). This warming triggered local soil-atmosphere feedbacks, with enhanced sensible heat flux and longwave radiation further energizing the atmospheric column (Jiang et al., 2023). The synergy of these thermodynamic processes culminated in extreme air temperatures and accelerated glacier melt throughout the 2022 summer in central-eastern TP.

The persistent TP anticyclone elevated air temperatures while suppressing precipitation across the central-western TP. The vertical overlap of the WPSH and SAH critically disrupted water vapor transport toward the central TP. This high-pressure regime further suppressed convective activity spanning from the Himalayas to southeastern and central TP, exacerbating regional precipitation deficits.

Under these sustained anticyclonic conditions, a distinct moisture circulation

https://doi.org/10.5194/egusphere-2025-2579
Preprint. Discussion started: 31 July 2025

anomaly with anticyclonic flow developed over the southwestern TP (Figure. 10). Weakened northwestward and northeastward moisture transport from the Indian Ocean and Arabian Sea induced pronounced moisture divergence over the central-western TP. Coupled with persistent anticyclonic forcing, these circulation dynamics collectively drove the observed precipitation reduction in the central TP during the 2022 heatwave.

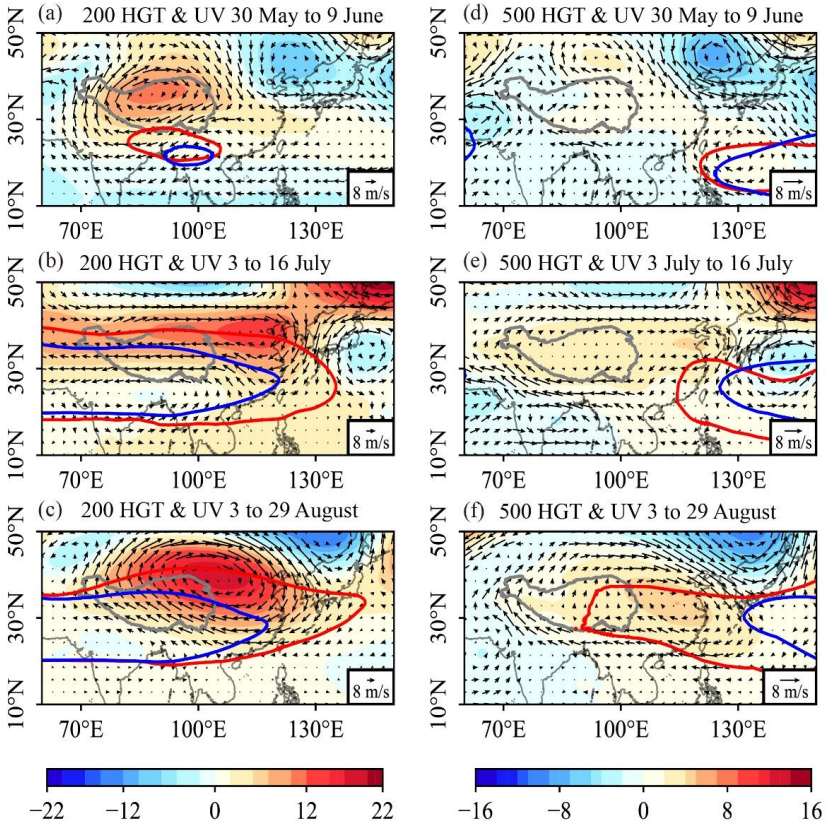

Figure 9. Spatial distribution of the geopotential height (shading) and horizontal wind (vector) at (a-c) (200 hPa) and (e-f) (500 hPa). The blue solid (dashed) contour in (a), (c) and (e) represents the 1250-gpm isopleth at the 200 hPa. The blue solid (dashed) contour in (b), (d) and (f) represents the 5880-gpm isopleth at the 500 hPa.

https://doi.org/10.5194/egusphere-2025-2579
Preprint. Discussion started: 31 July 2025

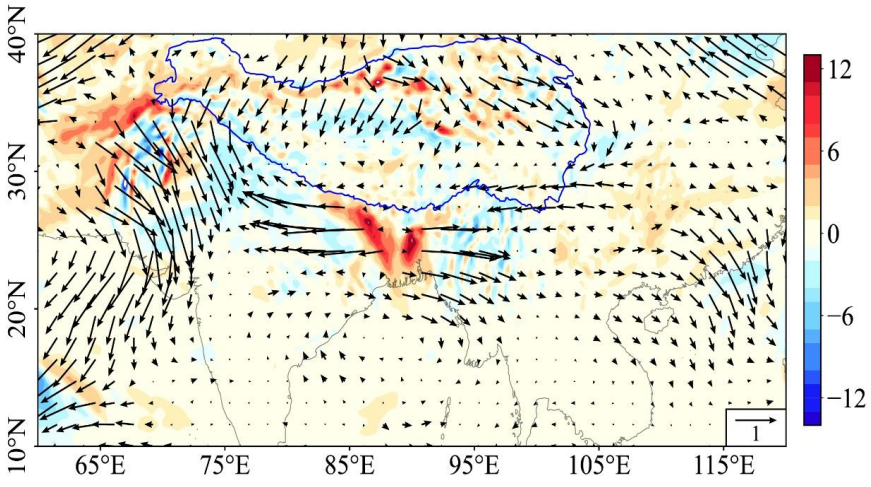

Figure 10. Spatial distribution of the vertically integrated water vapour flux (kg m^{-1} s^{-1}) and its divergence (shading; 10^{-5} kg·m^{-2} s^{-1}) anomalies during the three summer 2022 heatwave events.

Current studies have also examined drivers of the 2022 summer precipitation deficit over TP and eastern China from alternative perspectives. For instance, anomalous spring TP warming, associated with reduced snow cover, has been linked to the northeastward displacement of the SAH and northwestward migration of the WPSH (Li et al., 2023). Concurrently, this preseason warming weakened the southwest monsoon originating from the Bay of Bengal, enhanced the east–west sea surface temperature gradient in the Indian Ocean, and generated anomalous easterly winds along Indonesia's western coast (Cai et al., 2023).

Additionally, Antarctic warm anomalies shifted the Asian monsoon circulation southward, promoting water vapor convergence over Pakistan (Zhang et al., 2024). Jeong et al. (2023) further demonstrated that the co-occurrence of a negative Indian Ocean Dipole and La Niña during summer 2022 amplified rainfall in the northwestern Indian subcontinent and Pakistan while suppressing precipitation in southern China and the central TP. Collectively, interactions between large-scale circulation patterns and regional atmospheric anomalies drove the prolonged high temperatures, low precipitation and extreme melt events observed across the central TP from June to September 2022.

https://doi.org/10.5194/egusphere-2025-2579
Preprint. Discussion started: 31 July 2025

Recent studies have further investigated contributing factors to the 2022 summer precipitation deficit across TP and eastern China through complementary approaches. Spring TP warming anomalies - associated with diminished snow cover - have been shown to displace the SAH northeastward and shift the WPSH northwestward (Li et al., 2023). This preseason thermal anomaly concurrently weakened the Bay of Bengal-originating southwest monsoon, intensified the Indian Ocean's zonal sea surface temperature gradient, and generated anomalous easterlies along Indonesia's western coast (Cai et al., 2023). Antarctic thermal anomalies induced a southward meridional shift in Asian monsoon circulation, enhancing water vapor convergence over Pakistan (Zhang et al., 2024a). Jeong et al. (2023) established that the concurrent 2022 summer negative Indian Ocean Dipole and La Niña conditions amplified rainfall across the northwestern Indian subcontinent and Pakistan, while strongly suppressing precipitation in southern China and central TP.

The synergistic interplay between hemispheric-scale circulation patterns and regional atmospheric anomalies ultimately drove the extended period of elevated air temperatures, precipitation deficits, and extreme melt events observed across central TP from June to September 2022.

6.2 Hydrological Effects of Extreme Heatwaves and Glacial Melt Events

Extreme heatwaves and associated melting events significantly alter hydrological regimes in glacier-fed basins, triggering anomalous runoff surges and flood risks such as increased flood hazards. The seasonal occurrence of heatwaves influences ice-snow melting intensity and regulates meltwater contributions to total runoff through albedo-melt feedback mechanisms. Hydrological analyses reveal that glacial meltwater contributions to total runoff during 2022 heatwaves substantially exceeded baseline summer levels observed from 2019 to 2021 (Zhu et al., 2024a). The early-season heatwave (May 30 to June 9) initiated crucial cryosphere transformations: rapid snowpack depletion exposed underlying glacier ice, which lowered surface albedo and increased radiative energy absorption. These surface alterations prolonged albedo-melt feedback processes that interacted synergistically with subsequent July-

https://doi.org/10.5194/egusphere-2025-2579
Preprint. Discussion started: 31 July 2025

August heatwaves, resulting in cumulative melt amplification effects. Furthermore, the early-season heatwave accelerated the timing of snowmelt, diminishing the snowpack's capacity to sustain total runoff while potentially leading to seasonal drought conditions (Anderson et al., 2023). This dual impact - combining intensified glacier melt with reduced non-glacier snowpack contributions - fundamentally transformed basin-scale water budgets throughout June to September in the summer of 2022.

7. Conclusion

In this study, we combined multi-source data (October 2019 to September 2022) with a surface energy-mass balance model and a novel dual-threshold framework to identify extreme mass loss events in short-term glacier mass balance records on Sangqu Glacier, enabling a three-year analysis of energy-mass balance characteristics and melt mechanisms during heatwave events in the Geladandong region of the central Tibetan Plateau.

The EBFM can better capture the energy and mass balance processes of Sangqu Glacier. Measured and simulated values of albedo, incoming shortwave radiation, incoming/outgoing longwave radiation, point mass balance, and glacier-wide mass balance across elevations were in strong agreement. The energy and mass balances on the glacier surface are characterized by significant seasonal and interannual variations. Net shortwave and longwave radiation are the most important components of energy balance. Glacier surface energy and mass balances exhibit pronounced seasonal and interannual variability. Annual surface mass balance values for 2019–2020 (–540 mm w.e.) and 2020–2021 (–831 mm w.e.) contrast sharply with the extreme deficit of –1251 mm w.e. in 2021–2022, marking the most severe mass loss in the study period. Our dual-threshold detection method conclusively identified the extreme mass loss event at Sangqu Glacier, demonstrating its robustness in short-record contexts.

Compared to the 2019–2021 average melt, a 572 mm w.e. increase in mass loss was observed during the 2022 summer heatwaves. Melt during summer heatwaves

https://doi.org/10.5194/egusphere-2025-2579
Preprint. Discussion started: 31 July 2025

exhibited significantly higher frequency and intensity than melt during spring heatwaves (Zhu et al., 2024b), with 52 cumulative summer heatwave days producing 1,135 mm w.e. of melt—accounting for 65.2% of the total 2021–2022 melt. These melt events are associated with anomalously low albedo, high incoming longwave radiation, and sensible heat fluxes. Such anomalies in the energy balance were driven by large-scale atmospheric circulation anomalies—specifically, the concurrent intensification and westward expansion of the Western Pacific Subtropical High (WPSH) and the eastward extension of the South Asian High (SAH). This atmospheric circulation anomaly pattern induced high air temperatures via anticyclonic subsidence while causing reduced precipitation through suppressed moisture transport. Future research should extend the dual-threshold framework to other TP glaciers to evaluate its efficacy in detecting extreme melt events across diverse climatic regimes, while also prioritizing mechanistic analyses of how compound heatwave-drought interactions exacerbate glacier mass loss under projected climate warming.

Acknowledgements We thank the editor and anonymous reviewers for their constructive feedback on the manuscript, which led to substantial improvements during the review process.

Code and Data Availability Statement Meteorological data from the Tuotuohe meteorological station was obtained from the China Meteorological Administration's website (http://data.cma.cn/). ERA5 is available for download at https://cds.climate.copernicus.eu/cdsapp#!/search?type=dataset. The EBFM model is available via https://github.com/ wardvp/EBFM-glacier. The Dual-Threshold Framework can be found at https://github.com/zhuzhufeifei/detect_extreme_events. Data supporting the findings of this study are available from the corresponding author upon reasonable request.

Author contribution All authors contributed to the study conception and design. Data collection was performed by F. Z. Analysis was performed by F. Z, M. Z and L. A. The first draft of the manuscript was written by F. Z and all authors commented on

https://doi.org/10.5194/egusphere-2025-2579
Preprint. Discussion started: 31 July 2025

previous versions of the manuscript. All authors read and approved the final manuscript.

Competing interests: The authors declare that they have no conflict of interest.

Financial support This study was jointly funded by the National Key R&D Program of China (Grant No. 2024YFF0808302, 2024YFF0808601), the Science and Technology Projects of Xizang Autonomous Region, China (Grant No. XZ202501JD0025), and Second TP Scientific Expedition and Research Program (Grant No. 2019QZKK0201).

References

Anderson, S., & Radic, V. (2023). Modeling the Streamflow Response to Heatwaves Across Glacierized Basins in Southwestern Canada. *WATER RESOURCES RESEARCH*, *59*(12). https://doi.org/10.1029/2023WR035428

Beckmann J, Winkelmann R (2023) Effects of extreme melt events on ice flow and sea level rise of the Greenland Ice Sheet. The Cryosphere 17:3083–3099. https://doi.org/10.5194/tc-17-3083-2023

Bolch T, Kulkarni A, Kääb A, et al (2012) The State and Fate of Himalayan Glaciers. Science 336:310–314. https://doi.org/10.1126/science.1215828

Bougamont M, Bamber JL, Greuell W (2005) A surface mass balance model for the Greenland Ice Sheet. J Geophys Res 110:2005JF000348. https://doi.org/10.1029/2005JF000348

Brun F, Berthier E, Wagnon P, et al (2017) A spatially resolved estimate of High Mountain Asia glacier mass balances from 2000 to 2016. Nature Geosci 10:668–673. https://doi.org/10.1038/ngeo2999

Brunt D (1932) Notes on radiation in the atmosphere. I. Quart J Royal Meteoro Soc 58:389–420. https://doi.org/10.1002/qj.49705824704

Chen J, Xue X, Du W (2024) Short communication: Extreme glacier mass loss triggered by high temperature and drought during hydrological year 2022 / 2023 in Qilian Mountains. Research in Cold and Arid Regions 16:1–4. https://doi.org/10.1016/j.rcar.2024.01.002

Chen R, Li X (2023) Causes of the persistent merging of the western North Pacific subtropical high and the Iran high during late July 2022. Clim Dyn 61:2285–2297. https://doi.org/10.1007/s00382-023-06678-x

Duan J, Zhang H, Jian D, et al (2024) Influences of Anthropogenic Forcing on the Exceptionally Warm August 2022 over the Eastern Tibetan Plateau. Bulletin of the American Meteorological Society 105:E1068–E1073. https://doi.org/10.1175/BAMS-D-23-0179.1

Favier V, Wagnon P, Chazarin J, et al (2004) One-year measurements of surface heat budget on the ablation zone of Antizana Glacier 15, Ecuadorian Andes. J Geophys Res 109:2003JD004359. https://doi.org/10.1029/2003JD004359

Guo S, Chen R, Li H (2022) Surface Sublimation/Evaporation and Condensation/Deposition and Their Links to Westerlies During 2020 on the August-One Glacier, the Semi-Arid Qilian

https://doi.org/10.5194/egusphere-2025-2579
Preprint. Discussion started: 31 July 2025

Mountains of Northeast Tibetan Plateau. JGR Atmospheres 127:e2022JD036494. https://doi.org/10.1029/2022JD036494

Guo W, Liu S, Xu J, et al (2015) The second Chinese glacier inventory: data, methods and results. J Glaciol 61:357–372. https://doi.org/10.3189/2015JoG14J209

Hock R, Holmgren B (2005) A distributed surface energy-balance model for complex topography and its application to Storglaciären, Sweden. J Glaciol 51:25–36. https://doi.org/10.3189/172756505781829566

Hoffmann L, Günther G, Li D, et al (2019) From ERA-Interim to ERA5: the considerable impact of ECMWF's next-generation reanalysis on Lagrangian transport simulations. Atmos Chem Phys 19:3097–3124. https://doi.org/10.5194/acp-19-3097-2019

Hua W, Dai A, Qin M, et al (2023) How Unexpected Was the 2022 Summertime Heat Extremes in the Middle Reaches of the Yangtze River? Geophysical Research Letters 50:e2023GL104269. https://doi.org/10.1029/2023GL104269

Hugonnet R, McNabb R, Berthier E, et al (2021) Accelerated global glacier mass loss in the early twenty-first century. Nature 592:726–731. https://doi.org/10.1038/s41586-021-03436-z

Immerzeel WW, Lutz AF, Andrade M, et al (2020) Importance and vulnerability of the world's water towers. Nature 577:364–369. https://doi.org/10.1038/s41586-019-1822-y

Jeong H, Park H-S, Chowdary JS, Xie S-P (2023) Triple-Dip La Niña Contributes to Pakistan Flooding and Southern China Drought in Summer 2022. Bulletin of the American Meteorological Society 104:E1570–E1586. https://doi.org/10.1175/BAMS-D-23-0002.1

Kang S, Wang F, Morgenstern U, et al (2015) Dramatic loss of glacier accumulation area on the Tibetan Plateau revealed by ice core tritium and mercury records. The Cryosphere 9:1213–1222. https://doi.org/10.5194/tc-9-1213-2015

King O, Ghuffar S, Bhattacharya A, et al (2023) Glaciological and climatological drivers of heterogeneous glacier mass loss in the Tanggula Shan (Central-Eastern Tibetan Plateau), since the 1960s. J Glaciol 69:1149–1166. https://doi.org/10.1017/jog.2023.5

Kronenberg M, Van Pelt W, Machguth H, et al (2022) Long-term firn and mass balance modelling for Abramov Glacier in the data-scarce Pamir Alay. The Cryosphere 16:5001–5022. https://doi.org/10.5194/tc-16-5001-2022

Li N, Xiao Z, Zhao L (2021) A Recent Increase in Long-Lived Heatwaves in China Under the Joint Influence of South Asia and Western North Pacific Subtropical Highs. Journal of Climate 1–42. https://doi.org/10.1175/JCLI-D-21-0014.1

Li S, Yao T, Yang W, et al (2018) Glacier Energy and Mass Balance in the Inland Tibetan Plateau: Seasonal and Interannual Variability in Relation to Atmospheric Changes. JGR Atmospheres 123:6390–6409. https://doi.org/10.1029/2017JD028120

Li Z, Xiao Z, Ling J (2023) Impact of extremely warm Tibetan Plateau in spring on the rare rainfall anomaly pattern in the regions west and east to Plateau in late summer 2022. Atmospheric Research 290:106797. https://doi.org/10.1016/j.atmosres.2023.106797

Liang L, Cuo L, Liu Q (2019) Mass Balance Variation and Associative Climate Drivers for the Dongkemadi Glacier in the Central Tibetan Plateau. JGR Atmospheres 124:10814–10825. https://doi.org/10.1029/2019JD030615

(Lisette) Klok EJ, Oerlemans J (2002) Model study of the spatial distribution of the energy and mass balance of Morteratschgletscher, Switzerland. J Glaciol 48:505–518. https://doi.org/10.3189/172756502781831133

https://doi.org/10.5194/egusphere-2025-2579
Preprint. Discussion started: 31 July 2025

Liu W, Zhang D, Qin X, et al (2021) Monsoon Clouds Control the Summer Surface Energy Balance on East Rongbuk Glacier (6,523 m Above Sea Level), the Northern of Mt. Qomolangma (Everest). JGR Atmospheres 126:e2020JD033998. https://doi.org/10.1029/2020JD033998

Mölg T, Cullen NJ, Hardy DR, et al (2008) Mass balance of a slope glacier on Kilimanjaro and its sensitivity to climate. Intl Journal of Climatology 28:881–892. https://doi.org/10.1002/joc.1589

Oerlemans J, Knap WH (1998) A 1 year record of global radiation and albedo in the ablation zone of Morteratschgletscher, Switzerland. J Glaciol 44:231–238. https://doi.org/10.3189/S0022143000002574

Potocki M, Mayewski PA, Matthews T, et al (2022) Mt. Everest's highest glacier is a sentinel for accelerating ice loss. npj Clim Atmos Sci 5:7. https://doi.org/10.1038/s41612-022-00230-0

Pu J, Yao T, Yang M, et al (2008) Rapid decrease of mass balance observed in the Xiao (Lesser) Dongkemadi Glacier, in the central Tibetan Plateau. Hydrological Processes 22:2953–2958. https://doi.org/10.1002/hyp.6865

Raei E, Nikoo MR, AghaKouchak A, et al (2018) GHWR, a multi-method global heatwave and warm-spell record and toolbox. Sci Data 5:180206. https://doi.org/10.1038/sdata.2018.206

Reijmer CH, Hock R (2008) Internal accumulation on Storglaciären, Sweden, in a multi-layer snow model coupled to a distributed energy- and mass-balance model. J Glaciol 54:61–72. https://doi.org/10.3189/002214308784409161

Shan B, Verhoest NEC, De Baets B (2024) Identification of compound drought and heatwave events on a daily scale and across four seasons. Hydrol Earth Syst Sci 28:2065–2080. https://doi.org/10.5194/hess-28-2065-2024

Thibert E, Dkengne Sielenou P, Vionnet V, et al (2018) Causes of Glacier Melt Extremes in the Alps Since 1949. Geophysical Research Letters 45:817–825. https://doi.org/10.1002/2017GL076333

Tian L, Masson-Delmotte V, Stievenard M, et al (2001) Tibetan Plateau summer monsoon northward extent revealed by measurements of water stable isotopes. J Geophys Res 106:28081–28088. https://doi.org/10.1029/2001JD900186

Tian Y, Ghausi SA, Zhang Y, et al (2023) Radiation as the dominant cause of high-temperature extremes on the eastern Tibetan Plateau. Environ Res Lett 18:074007. https://doi.org/10.1088/1748-9326/acd805

Van Pelt W, Pohjola V, Pettersson R, et al (2019) A long-term dataset of climatic mass balance, snow conditions, and runoff in Svalbard (1957–2018). The Cryosphere 13:2259–2280. https://doi.org/10.5194/tc-13-2259-2019

Van Pelt WJJ, Oerlemans J, Reijmer CH, et al (2012) Simulating melt, runoff and refreezing on Nordenskiöldbreen, Svalbard, using a coupled snow and energy balance model. The Cryosphere 6:641–659. https://doi.org/10.5194/tc-6-641-2012

Vargo, L. J., Anderson, B. M., Dadić, R., Horgan, H. J., Mackintosh, A. N., King, A. D., & Lorrey, A. M. (2020). Anthropogenic warming forces extreme annual glacier mass loss. Nature Climate Change, 10(9), 856–861. https://doi.org/10.1038/s41558-020-0849-2

Wei Lele, He Xiaobo, Xue Yu'ang, Wang Shaoyong, Guo Haonan, Ding Yongjian, & Yao Tandong. (2025). Analysis of the characteristics of Xiao Dongkemadi Glacier mass balance

https://doi.org/10.5194/egusphere-2025-2579
Preprint. Discussion started: 31 July 2025

changes in Tanggula Mountains from 2005 to 2023. *Journal of Glaciology and Geocryology*, *47*(2), 317–329.

Xu C, Li H, Wang F, et al (2024) Heatwaves in summer 2022 forces substantial mass loss for Urumqi Glacier No. 1, China. Journal of Glaciology 70:e77. https://doi.org/10.1017/jog.2024.4

Yan R, Wang X, Wang J, et al (2024) Warm Early Summer Compensated Reduction in Photosynthesis Caused by 2022 Late Summer Extreme Drought Over the Tibetan Plateau. Journal of Geophysical Research: Biogeosciences 129:e2023JG007859. https://doi.org/10.1029/2023JG007859

Yang W, Yao T, Guo X, et al (2013) Mass balance of a maritime glacier on the southeast Tibetan Plateau and its climatic sensitivity. JGR Atmospheres 118:9579–9594. https://doi.org/10.1002/jgrd.50760

Yao T, Bolch T, Chen D, et al (2022) The imbalance of the Asian water tower. Nat Rev Earth Environ 3:618–632. https://doi.org/10.1038/s43017-022-00299-4

Yao T, Masson-Delmotte V, Gao J, et al (2013) A review of climatic controls on δ^{18} O in precipitation over the Tibetan Plateau: Observations and simulations. Reviews of Geophysics 51:525–548. https://doi.org/10.1002/rog.20023

Yao T, Thompson L, Yang W, et al (2012) Different glacier status with atmospheric circulations in Tibetan Plateau and surroundings. Nature Clim Change 2:663–667. https://doi.org/10.1038/nclimate1580

You Q, Wu F, Shen L, et al (2020) Tibetan Plateau amplification of climate extremes under global warming of 1.5 °C, 2 °C and 3 °C. Global and Planetary Change 192:103261. https://doi.org/10.1016/j.gloplacha.2020.103261

Zhang T, Deng Y, Chen J, et al (2023a) An energetics tale of the 2022 mega-heatwave over central-eastern China. npj Clim Atmos Sci 6:162. https://doi.org/10.1038/s41612-023-00490-4

Zhang T, Wang W, An B, Wei L (2023b) Enhanced glacial lake activity threatens numerous communities and infrastructure in the Third Pole. Nat Commun 14:8250. https://doi.org/10.1038/s41467-023-44123-z

Zhang J, Chen H, Fang X, et al (2024) Warming-induced hydrothermal anomaly over the Earth's three Poles amplifies concurrent extremes in 2022. npj Clim Atmos Sci 7:8. https://doi.org/10.1038/s41612-023-00553-6

Zhou B, Zhai P, Liao Z (2024) Bivariate attribution of the compound hot and dry summer of 2022 on the Tibetan Plateau. Sci China Earth Sci 67:2122–2136. https://doi.org/10.1007/s11430-023-1320-y

Zhu F, Zhu M, Guo Y, Yao T (2024a) Observation and Simulation of Runoff During an Extreme Heatwave in a Glacial Basin on the Central Tibetan Plateau. Hydrological Processes 38:e70014. https://doi.org/10.1002/hyp.70014

Zhu F, Zhu M, Yang W, et al (2024b) Drivers of the Extreme Early Spring Glacier Melt of 2022 on the Central Tibetan Plateau. Earth and Space Science 11:e2023EA003297. https://doi.org/10.1029/2023EA003297

Zhu M, Thompson LG, Yao T, et al (2023) Opposite mass balance variations between glaciers in western Tibet and the western Tien Shan. Global and Planetary Change 220:103997. https://doi.org/10.1016/j.gloplacha.2022.103997

https://doi.org/10.5194/egusphere-2025-2579
Preprint. Discussion started: 31 July 2025

Zhu M, Thompson LG, Zhao H, et al (2021) Influence of atmospheric circulation on glacier mass balance in western Tibet: an analysis based on observations and modeling. Journal of Climate 1–55. https://doi.org/10.1175/JCLI-D-20-0988.1

Zhu M, Yao T, Xie Y, et al (2020) Mass balance of Muji Glacier, northeastern Pamir, and its controlling climate factors. Journal of Hydrology 590:125447. https://doi.org/10.1016/j.jhydrol.2020.125447

Zhu M, Yao T, Yang W, et al (2018) Differences in mass balance behavior for three glaciers from different climatic regions on the Tibetan Plateau. Clim Dyn 50:3457–3484. https://doi.org/10.1007/s00382-017-3817-4

Zhu, M., Yao, T., Thompson, L. G., Wang, S., Yang, W., & Zhao, H. (2022a). What induces the spatiotemporal variability of glacier mass balance across the Qilian Mountains. *Climate Dynamics*, *59*(11–12), 3555–3577. https://doi.org/10.1007/s00382-022-06283-4

Zhu M, Yao T, Yang W, et al (2022b) Possible Causes of Anomalous Glacier Mass Balance in the Western Kunlun Mountains. JGR Atmospheres 127:e2021JD035705. https://doi.org/10.1029/2021JD035705

Appendix

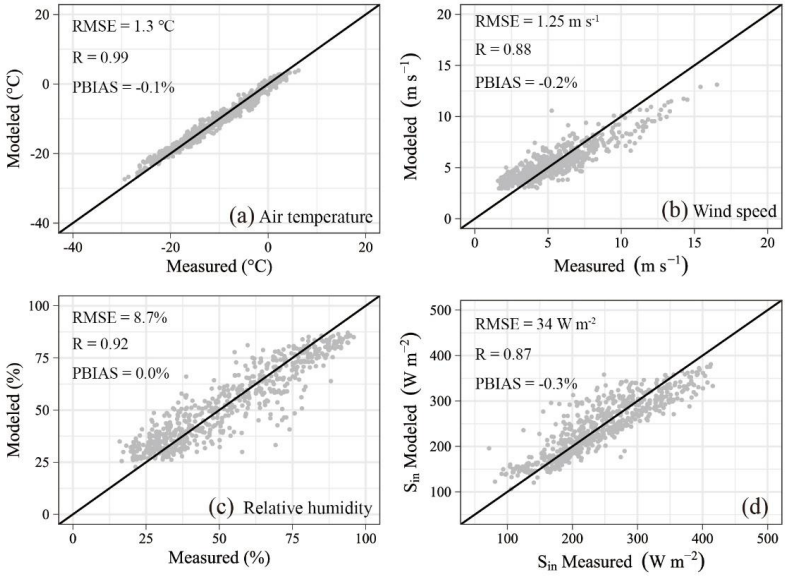

Figure A1. Comparison of observed and ERA5 downscaled (a) Air temperature, (b) Relative humidity, (c) Wind speed, and (d) Incoming shortwave radiation at the daily scale.

https://doi.org/10.5194/egusphere-2025-2579
Preprint. Discussion started: 31 July 2025

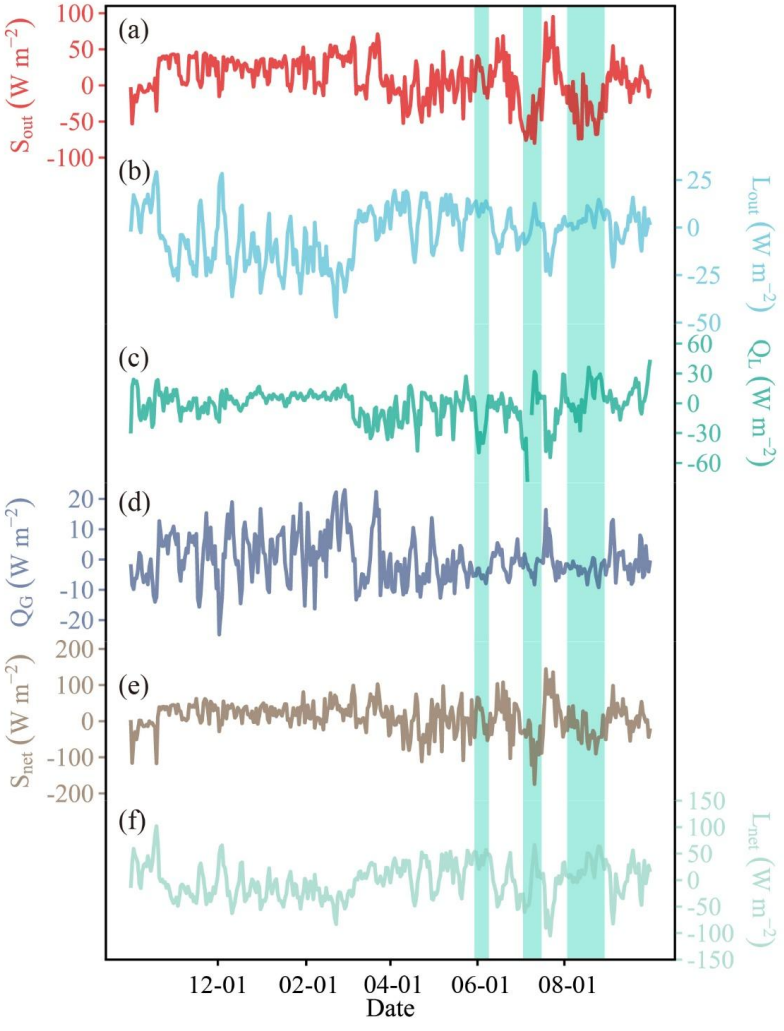

Figure A2. Energy balance components associated with the glacier melt events in summer 2022. Anomalous (a) Outgoing shortwave radiation, (b) Outgoing longwave radiation, (c) Latent heat fluxes, (d) Snow and ice heat flux, (e) Net shortwave radiation, and (f) Net longwave radiation from October 2021 to October 2022 (reference period is October 2019–September 2021). Color shading represents extreme heat waves.